ADVANCED FUNCTIONAL MATERIALS
www.afm-journal.de

Transparent Cellulose Aerogels from Concentrated Salt Solutions: Synthesis and Characterization

Baldur Schroeter, Sven Holst, Isabella Jung, Lara Gibowsky, Raman Subrahmanyam, Pavel Gurikov, and Irina Smirnova*

In this work, nanostructured and transparent cellulose aerogels are synthesized via a purely salt induced approach from non-modified microcrystalline cellulose type II. The production process requires in contrast to state of the art methods no pretreatment of cellulose or use of expensive cellulose-solvents: it consists of hydrogel formation via cross-linking of cellulose with calcium ions, a solvent exchange and a supercritical drying step. A systematic multiparameter study reveals that a high level of structural control is achievable: ratios of macro- to mesoporosity and the size of mesopores can be tailored by adjustment of the calcium ion content, while keeping a high overall porosity in the range of 92% – 96 %. The build-up of homogeneous, fine pore structures results in a significant increase of the specific surface area as compared to conventional calcium-free aerogels (684 vs. 300 $m^2\ g^{-1}$). Remarkably, the Ca^{2+}-cross-linking renders aerogels transparent, with Rayleigh scattering being the dominant scattering mechanism. Additional ion exchange to Ca^{2+} in the hydrogel-state leads to further reduction of the pore size and to products with optimized optical properties, e.g., light transmission of 91% at an incidents light wavelength of 800 nm and a substrate thickness of 1.5 mm.

1. Introduction

Due to their outstanding properties, aerogels have been listed as IUPAC top ten emerging technologies in chemistry 2022.[1] Their applicability is derived from unique microstructural attributes, namely high mesopore volumes as well as overall porosities (up to 99%) which result in high mass specific surface areas S_m (up to ≈1200 $m^2\ g^{-1}$) and low densities (≈ 0.001 – 0.2 g cm^{-3}). Combination of these properties with optical transparency opens up attractive application avenues, e.g. as transparent insulators in advanced glazing units, skylights and energy saving windows, and is – up to now – mainly governed by silica aerogels.[2–4] Nevertheless, brittleness and fragility caused by silica aerogel´s nanocolloidal structure limits the commercial applicability.[3,5] A rising trend is the use of biopolymer aerogels, which show enhanced mechanical properties, abundant availability of starting materials and superior biocompatibility. Their properties are rooted in their foam-like, fibrillar morphologies build-up from three-dimensionally entangled micro- and nanofibers.[6,7] These micro- and nanostructures are often comprised of a wide variety of pore and building block sizes and thus fail in many cases to meet the requirements which are necessary to avoid light scattering.

Minimization of scattering events during light transmittance, thus suppression of Mie scattering and substantial reduction of Rayleigh scattering are necessary to obtain transparent nanoporous materials.[8] The dominating scattering mechanism depends on the ratio of scatter size and wavelength λ of the incident light, resulting in Mie scattering for scatter sizes greater than λ and Rayleigh scattering if the scatter size is smaller than ≈ 1/10 λ.[9] Both types of scattering are caused by interaction of light with the aerogel structure, in particular by interaction of light with spatial inhomogeneities of the refractive index n, which occur due to the porous nature of the material.[4,10,11] Transparent aerogels should therefore contain no micrometer-sized pores and other structural features like particles, fibers and defects. If these prerequisites are met, Rayleigh scattering contributes predominantly to the loss of transparency. Rayleigh scattering intensity shows high dependencies on the scatters diameter (to the power of six in case of spherical objects) as well as on the wavelength of the incident light (to the power of 4).[4,10] In case of light within the visible range, Rayleigh scattering becomes negligible for structures below ≈ 50 nm.[10]

Synthesis of biopolymer aerogels with sufficient homogeneity and structural features solely below 50 nm poses challenges

B. Schroeter, S. Holst, I. Jung, L. Gibowsky, I. Smirnova
Institute for Thermal Separation Processes
Hamburg University of Technology
Eißendorfer Straße 38, 21073 Hamburg, Germany
E-mail: baldur.schroeter@tuhh.de
R. Subrahmanyam
aerogel-it GmbH
Albert-Einstein-Str. 1, 49076 Osnabrück, Germany
P. Gurikov
Laboratory for Development and Modelling of Novel Nanoporous Materials
Hamburg University of Technology
Eißendorfer Straße 38, 21073 Hamburg, Germany
The ORCID identification number(s) for the author(s) of this article can be found under https://doi.org/10.1002/adfm.202407547

DOI: 10.1002/adfm.202407547

in each step of the production process. For instance, build-up of 3D pore networks can be started from biopolymer solutions by crosslinking or coagulation of biopolymer molecule chains (molecular approach).[7] In coagulation of a biopolymer solution in a non-solvent, the kinetics of phase separation and the interactions between biopolymer and non-solvent play decisive roles. Structural control is not easy achievable and resulting multiscale pore networks contain often a significant macropore content.[12] Alternatively, gelation can also be triggered via covalent or ionic crosslinking of dissolved cellulose.[7] Regardless of the gelation mechanism, macroscopic phase separation has to be suppressed during gel formation in order to achieve homogeneous and fine structures.[10,13] The subsequent removal of liquids from the wet gels under preservation of the nanostructure is generally achievable by a solvent exchange from water to an organic solvent followed by supercritical CO_2-drying. A stepwise solvent exchange, high crosslinking degree and high biopolymer concentration are found to be useful to mitigate the problem of gel shrinkage during these steps, e.g., as reported for Ca^{2+}-crosslinked alginate aerogels.[14,15]

Considering aforementioned aspects, it is not surprising that synthesis of transparent biopolymer aerogels remains a major challenge in the field and is up to now covered only by several works which are limited to chitosan and cellulose-based materials. A fundamental breakthrough was achieved by Takeshita et al. in 2015 by preparing flexible, highly porous (up to ≈ 97%), transparent chitosan aerogels with high specific surface areas (up to 545 $m^2\ g^{-1}$) and low thermal conductivity (≈ 0.022 $W\ m^{-1}\ K^{-1}$) via covalent crosslinking of chitosan.[16–18] In comparison to chitosan, crosslinking of cellulose poses additional challenges, since cellulose contains besides -OH (and reducing ends) no reactive functional groups.

Overall, there are currently only a limited number of studies on non-hybrid, transparent cellulose aerogels and, because cellulose is not easily dissolvable, expensive or caustic solvents like ionic liquids (e.g. 1-Allyl-3-methyl-imidazoliumchlorid, AMIMCl) or cold alkali/water mixtures (≈ –9 °C) have to be employed in the molecular approach.[7,12,19–26]

In contrast to molecular based approaches, production of transparent cellulose aerogels is also possible via gelation of dispersed cellulose nanofibres (CNFs). While the use of cellulose-solvents is not required in this approach, grinding and separation steps are needed to obtain CNFs with desired properties and several cellulose pre-oxidation steps (e.g. by use of 2,2,6,6-tetramethylpiperidin-1-yl)oxidanyl, TEMPO) are usually necessary.[27–30] Recently, Abraham et al. successfully synthesized flexible, hydrophobic and highly transparent (visible light transmission up to 99%) cellulose aerogels with low thermal conductivity (down to ≈ 0.016 $W\ m^{-1}\ K^{-1}$) and sufficient thickness (range of few mm) from TEMPO oxidized CNFs.[30] While this work paved the way toward transparent cellulose aerogels with excellent properties, an elaborate oxidation procedure of cellulose fibers had to be carried out, including repetitive grinding and numerous oxidation/filtration and washing steps. Exceptions in which oxidation of cellulose CNFs and use of supercritical drying are not necessary are so far limited to the production of thin aerogel-films and membranes (thickness ≤ 200 µm).[31,32] To avoid the use of non-green solvents in the molecular approach as well as of oxidants and mechanical cellulose pre-treatment in the CNF-route, the use of inorganic molten salt hydrates as cellulose solvent can be considered, since they offer several attractive characteristics such as simple preparation in aqueous media, cost-effectiveness as well as recoverability of the salt.[21,33] One example is the use of bivalent zinc-ions (Zn^{2+}), which are well known for use in cellulose dissolution and fiber production, with earliest patents going back to the 19th century.[34] The use of $ZnCl_2 \cdot 4\ H_2O$ as a solvent for cellulose aerogel production was lately reported by Schestakow et al. and Rege et al.[34,35] Aerogels obtained after coagulation of $ZnCl_2/H_2O$/cellulose solutions (Zn-Cell) in cellulose non-solvents (e.g., acetone, 2-propanol and water) exhibited fibrillar, meso- to macroporous structures, which results in opaque appearance.

Lately, state-switchable, transparent cellulose hydrogels were fabricated via ion exchange between Zn^{2+} and Ca^{2+} from molten salt hydrates.[36,37] It was found that an increase of the Ca^{2+}-content in the gel leads to cellulose crosslinking and chain orientation, while Zn^{2+}-ions contribute to an increase in fluidity and low orientation.[38] This positive contribution of Ca^{2+}-ions to structural control is rooted in a high binding energy and high electron transfer tendency between Ca^{2+}-ions and the entire cellulose chains which enables Ca^{2+} to promote junction zones between adjacent cellulose chains.[37–39] Consequently, we regard crosslinking of cellulose via ion exchange of Zn^{2+} to Ca^{2+} as a promising approach toward ultimate structural control in cellulose aerogels and aim to explore the suitability of this purely salt induced route to prepare Ca^{2+}-cross-linked, transparent cellulose aerogels from non-modified, microcrystalline cellulose type II.

2. Results and Discussion

In this study, the cellulose content c_{cell} in the sol (c_{cell} = 3.25–6.00 wt.%, four levels) and concentrations of calcium ions c_{Ca2+} in the gelation bath ($c_{Ca2+,}$ 0 – 6.5 mol L^{-1}, five levels) were varied. The production of hydrogel discs was facilitated by immersion of Zn-Cell solutions in aqueous gelation solutions. While gel formation occurs immediately upon contact between the sol and the gelation solutions, different processes may dominate the arising hydrogels microstructure depending on the process settings (**Figure 1**): a) Diffusion of water into the emerging cellulose network, resulting in washing out of Zn^{2+}-ions and re-formation of hydrogen bonds between adjacent cellulose chains (coagulation); b) Diffusion of Ca^{2+} into the emerging cellulose network resulting in crosslinking due to cellulose-Ca^{2+} interactions (gelation); c) Furthermore, additional ion exchange between Zn^{2+} and Ca^{2+} is also possible after the primary gel body has been formed.[38] An interplay between these processes is depicted in Figure 1 and discussed in details with regard to textural (section 2.1) and optical properties (section 2.2).

2.1. Effect of Ion Content and Cellulose Concentration on Textural Properties

Textural changes induced by variation of the process parameters resulted in aerogel substrates with different optical appearances (section 2.2) and physical properties (summarized in Table S2, Supporting Information). At lower calcium ion concentrations (c_{Ca2+} = 0 – 2.6 mol L^{-1}), substrates with low cellulose amount

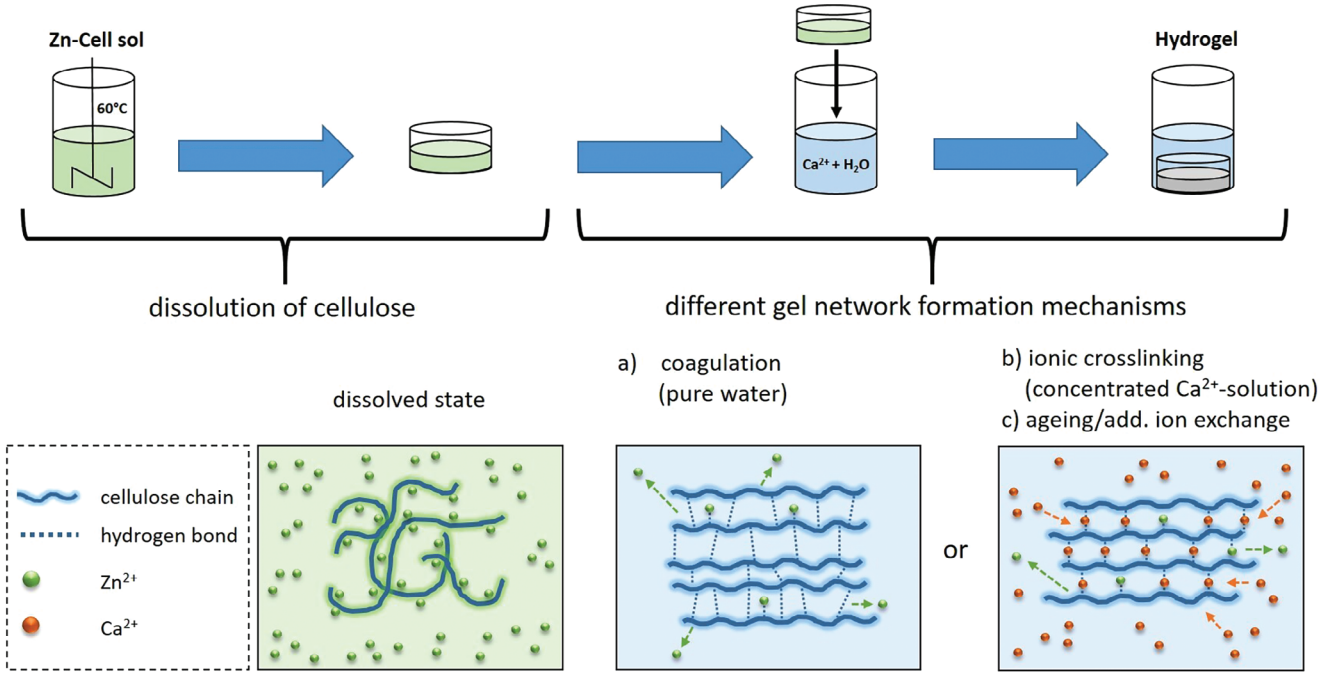

Figure 1. Schematic representation of cellulose hydrogel-slab production and cellulose solubilization/crosslinking/coagulation on a molecular level. After hydrogel formation a direct solvent exchange with ethanol and supercritical drying with CO_2 leads to the according aerogels.

in the sol ($c_{cell,low}$ = 3.25 – 4.00 wt.%) broke down to pieces during processing, while intact discs were obtainable using higher amounts of cellulose ($c_{cell,high}$ = 5.00 – 6.00 wt.%). Self-supporting substrates were generally obtained in the higher calcium ion concentration range ($c_{Ca2+} \geq 3.9$ mol L^{-1}) at all cellulose concentrations. Envelope densities ($\rho_e \approx 0.1 - 0.2$ g cm^{-3}) were in the same range as reported in previous works on Zn-cell based aerogels coagulated in different cellulose non-solvents (water, ethanol, isopropanol) and similar range of c_{cell}.[34,35] Overall porosities (ϵ = 92% – 96%) as estimated for all self-supporting samples showed as expected a slight dependence on c_{cell}, because an increase of the solid fraction resulted in an increase of ρ_e and therefore in a decrease of ϵ (Figure S5, Supporting Information). Skeletal densities were not significantly affected by process conditions ($\rho_{s,\,average}$ = 2.25 ± 0.26 g cm^{-3}). It is notable, that almost no volumetric shrinkage took place during solvent exchange (ΔV_{alco} < 6%), while in case of c_{Ca2+} > 3.9 mol L^{-1} even slight swelling was observed (Figure S6, Supporting Information). Shrinkage after the supercritical CO_2-drying ΔV_{aero} was in the typical range reported for aerogels coagulated from cellulose II with comparable solid content (ΔV_{aero}, = 23% – 51%).[12] In our case, ΔV_{aero} was only slightly influenced by c_{cell} and showed a clear dependence on the amount of calcium ions used for crosslinking, as is particularly illustrated by the trend of ΔV_{aero} in the range of c_{Ca2+} = 3.9 – 6.5 mol L^{-1} (Figure S6, Supporting Information): an increase of c_{Ca2+} results in a mitigation of shrinkage at high calcium ion concentrations, pointing to a positive contribution of multivalent crosslinking to the gels ability to withstand the supercritical drying step.

Overall, a wide range of different microstructures is accessible by variation of c_{cell} and c_{Ca2+}: associated changes of the mass specific surface area S_m, the mesopore volume V_{meso} and the mean mesopore diameter $d_{pore,mean}$ were estimated based on the results of nitrogen physisorption measurements. Since the assessable range of pore sizes in nitrogen physisorption is limited to mesopores (pore diameter d_{pore} = 2–50 nm) and biopolymer aerogels may contain also larger macropores (d_{pore} > 50 nm), it is important to note that only part of the overall porosity can be assessed by BET and BJH methods.[40] Assuming no contribution of micropores (d_{pore} < 2 nm), the macropore volume V_{macro} was estimated via:

$$V_{macro} = \frac{1}{\rho_e} - V_{meso} \quad (1)$$

Influence of c_{Ca2+} on the textural properties, both specific surface area and the mesopore volume, of resulting aerogels is given in **Figure 2**a. In comparison to gels obtained via coagulation in Ca^{2+}-free water ($S_m \approx 300$ m^2 g^{-1}), crosslinking of Zn-cell sol with Ca^{2+} leads to an increase of S_m up to ≈ 650 m^2 g^{-1}. Overall, S_m follows an exponential relation (R^2 0.998) in dependence of c_{Ca2+}:

$$S_m = 248.3 + 24.6 \cdot e^{(0.416 \cdot c_{Ca2+})} \quad (2)$$

Plausible reasons for the increase in the specific surface are: a) the formation of new mesoporous voids via Ca^{2+}–crosslinking; b) further Ca^{2+}-induced changes on a nanoscale level, e.g., due to changes of nanofibril diameters or agglomeration which might affect the mesopore sizes (and consequently also the BET surface area). In this picture, option a) leads to an increase of the specific surface area and mesopore volume, while for option b) an increase of the mesopore volume is not necessarily expected. The observation that V_{meso} is constant in certain ranges (c_{Ca2+} ≈ 0.0 – 2.6 and 5.2 – 6.5 mol L^{-1}) indicates indeed that different

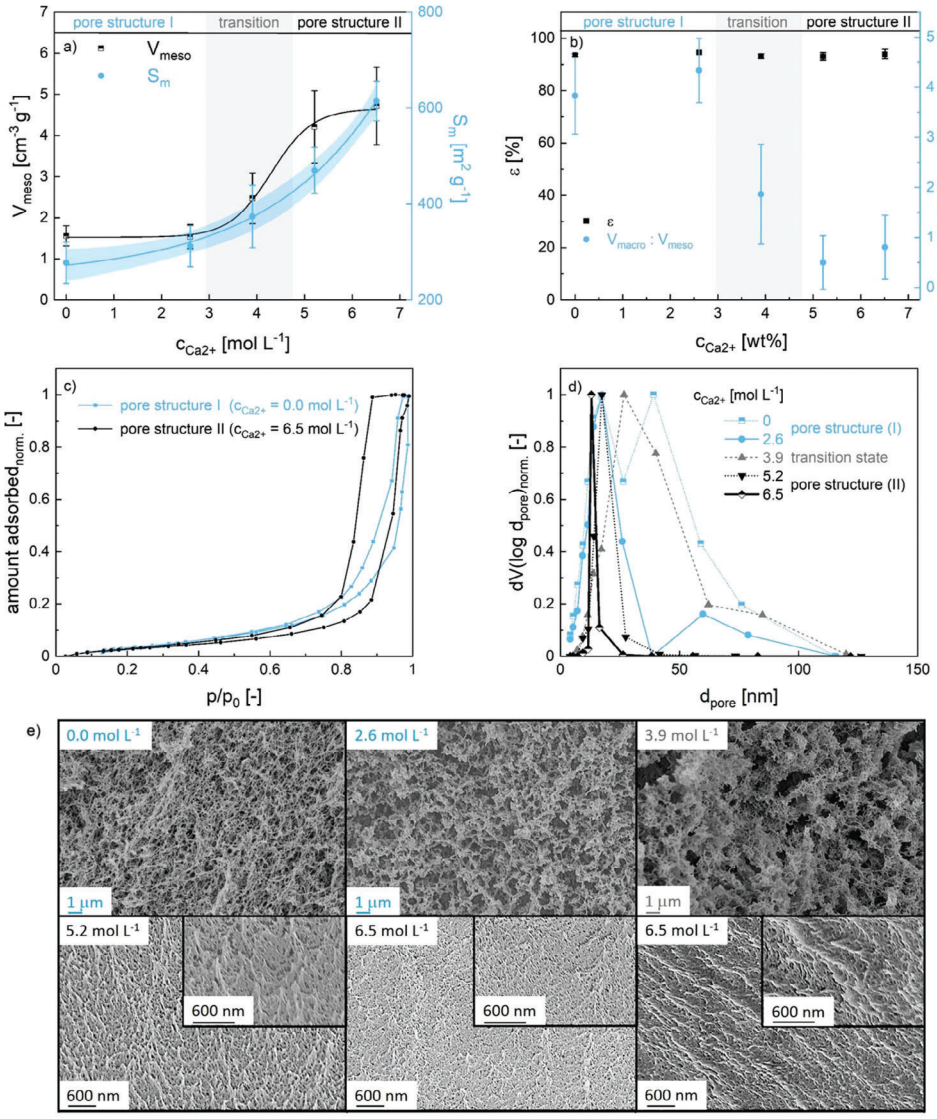

Figure 2. a) Specific surface area S_m and pore volume V_{meso} of cellulose aerogels in dependence of c_{Ca2+}. The straight blue line corresponds to exponential fitting, hatched area represents the 95% confidence interval. The black line is drawn to guide the eye. b) porosity ϵ and ratio V_{macro}: V_{meso} of cellulose aerogels in dependence of c_{Ca2+}. All values in figures a) and b) are averaged across all different cellulose concentrations (n = 4). Error bars correspond to the standard deviation around the mean values. c) Selected BJH isotherms obtained at c_{Ca2+} = 0 and 6.5 mol L^{-1} d) Normalized pore size distributions at different levels of c_{Ca2+} and at constant c_{cell} (5.00 wt.%). Lines are drawn to guide the eye. e) SEM pictures of corresponding aerogel microstructures. Concentration values refer to c_{Ca2+}.

effects are responsible for the buildup of specific surface area as c_{Ca2+} increases. Since we can consider the porosity to be largely constant in the entire range of c_{Ca2+}, an increase of V_{meso} is always associated with a loss of V_{macro}: hence we can state that increasing c_{Ca2+} does not lead to creation of new porous space, but to the formation of smaller pores instead of larger ones as reflected by the ratio of V_{macro}: V_{meso} (Figure 2b).

Following this general description, we can qualitatively classify aerogels obtained in this work into three categories: mainly macroporous systems obtained in the low range of c_{Ca2+} (pore structure I), predominantly mesoporous systems in the high range of c_{Ca2+} (pore structure II) and a transition state at c_{Ca2+} ≈ 3.9 mol L^{-1} (Figure 2a,b).

A more detailed description is provided from the estimation of pore size distributions via BJH method and from SEM imaging. In the following we address first changes related to the different Ca^{2+}-concentrations in the gelation bath at all cellulose contents in the sol (general trends), and discuss the influence of overall metal ion content in the aerogels regarding c_{cell} subsequently.

In absence and in the low concentration range of Ca^{2+} (c_{Ca2+} ≤ 2.6 mol L^{-1}), the pore structure is primarily being formed via non-solvent induced cellulose coagulation (V_{meso} = constant, pore structure I). The hysteresis loops observed in physisorption isotherms exhibit an H3-type pattern, indicating the presence of macropores that are not entirely filled with pore condensate (Figure 2c).[41] Gels coagulated in pure water show relatively

broad mesopore size distributions (Figure 2d; Figure S7, Supporting Information) and continuous macro- to mesoporous fibrous cellulose networks (as being typically observed in non-solvent coagulated and Zn-Cell based cellulose aerogels) are visible in SEM pictures (Figure 2e; Figures S8–S10, Supporting Information).[12,34,35,42] Increasing c_{Ca2+} to 2.6 mol L^{-1} seems then to result in an agglomeration of primary fibers (Figure 2e; Figures S8–S10, Supporting Information). The BET/BJH data suggests that some of the larger mesopores shrink during this process, as reflected in: a narrowing of pore size distributions (Figure 2d; Figure S7, Supporting Information), a shift of the mean pore diameter to lower values and associated slight increase of S_m (Figure 2a).

In the range of c_{Ca2+}≈3.9 mol L^{-1}, the calcium ion concentration is sufficient to interconnect spatially distant cellulose fibers (transition state). This is reflected in formation of mesoporous and fibrous clusters with higher cellulose (fiber) density as being visible in SEM pictures, whereas the relocation of cellulose in the system generates also larger (≈ 1 µm) macroporous voids (Figure 2e; Figures S8–S10, Supporting Information). BET/BJH analysis shows that additional cross-linking leads to a significant increase of the mesopore volume while no uniform trend can be observed in pore size distributions (Figure 2d; Figure S7, Supporting Information). Summarized, the transition state represents a high degree of spatial inhomogeneity with respect to the cellulose density distribution in the systems; textural properties of the aerogels obtained in the transition state are highly dependent on the individual ratio of c_{cell} to c_{Ca2+}.

At high concentrations of c_{Ca2+} (c_{Ca2+} = 5.2 – 6.5 mol L^{-1}), the pore network formation is dominated by Ca^{2+}-cross-linking, resulting in mainly mesoporous systems (pore structure II) with a significantly increased mesopore volume, which is accompanied by narrowing of pore size distribution, decrease of pore size and change of optical appearance (see section 2.2). A further shift of mesopores to smaller sizes and an increase of V_{meso} may contribute to the significant increase of specific surface area up to a maximum of S_m = 655 m^2 g^{-1} when increasing c_{Ca2+} from 5.2 to 6.5 mol L^{-1}. Comparing physisorption isotherms for the pore structures I and II, it is remarkable that the hysteresis loop for the pore structure II resembles H1 type (Figure 2c; Figure S3, Supporting Information).[41] This type is typical for materials which exhibit a narrow range of uniform mesopores and has so far been found for e.g. controlled pore glasses or templated silicas, but not for cellulose aerogels.[41] Homogenous morphologies containing uniform and small mesopores < 20 nm are indeed visible in SEM pictures (Figure 2e; Figures S8–S10, Supporting Information), whereas mesopores are distributed in oriented cellulose layers. Analogous layers have been observed in hydrogels produced at a comparable concentration of Ca^{2+} (c_{Ca2+} = 5.8 mol L^{-1}), indicating that crosslinking the Zn-Cell sol with Ca^{2+} results in the alignment of cellulose chains and the formation of anisotropic structures.[38] In our case, similar structures are still present after solvent exchange and supercritical drying steps.

While results presented above demonstrate the possibilities to manipulate the microstructures of Zn-Cell derived aerogels to a large extend by variation of c_{Ca2+}, relations between the calcium ion concentration in the gelation bath and textural properties provide only insights from a processing point of view. A deeper understanding about the influence of different ions and c_{Cell} on textural properties is achievable by relating the amount of remaining ions in the final aerogels (expressed as weight content in the aerogels, w_{M2+}). Both, w_{Ca2+} and w_{Zn2+} increase with increasing c_{Ca2+} (**Figure 3a**, Table S2, Supporting Information), showing that no complete ion exchange from Zn^{2+} to Ca^{2+} was achieved in the production process.

Moreover, a significant amount of ions stays coordinated inside the cellulose matrix during the solvent exchange step, which is consistent with former reports about ethanol not being able to remove coordinated Zn^{2+}-ions from cellulose matrices.[36,37] The total ion content in the final aerogels as well as ratios between the weight contents of Ca^{2+} to Zn^{2+} at a given c_{Ca2+} in the gelation solution are also related to c_{cell}: aerogels derived at lower cellulose concentrations ($c_{cell,low}$ = 3.25 – 4.00 wt.%) contain Zn^{2+} and Ca^{2+} ions in approximately equal mass proportions, and the use of higher cellulose concentrations ($c_{cell,high}$ = 5.00 – 6.00 wt.%) leads to calcium-enriched aerogels (see Figure 3a, Table S2, Supporting Information). Furthermore, the use of higher cellulose concentrations results in gels with a lower overall ion content (Δw_{M2+} = –2.3 ± 1.0 wt.% on average).

Due to production procedure used in this study (high amount of salts and absence of washing steps besides solvent exchange), it is interesting to elucidate, if residual salt crystals remain inside the samples, or if the entire value of w_{M2+} is incorporated into the cellulose chains contributing to the formation of the network. Indication can be provided by the use of the corrected envelope density without shrinkage $\rho_{e,corr}$:

$$\rho_{e,\,corr} = \rho_e \left(1 - \frac{\Delta V_{aero}}{V_0}\right) \quad (3)$$

with V_0 being the volume of the initial hydrogel and ΔV_{aero} the volumetric shrinkage from hydro- to aerogel.[34,43] In case of residues-free cellulose aerogels, the corrected envelope density is linearly correlated to c_{cell} and shows an intercept value of zero.[34,44] If metal ions are coordinated between cellulose molecule chains and are therefore part of the pore walls, the total solid content (s_{total}) concentration has to be used:

$$s_{total} = c_{cell} + \left(\frac{w_{M2+}}{100}\right) \quad (4)$$

In our case, linear correlation between $\rho_{e,corr}$ and s_{total} shows no remaining offset (intercept value = $-3.3\cdot10^{-3}\pm1.3\cdot10^{-2}$ g cm^{-3}, Figure 3b), which implies that the complete ion content in the gels is part of the pore network and that the systems contain no salt crystals/residuals. This result is supported by SEM images, where no salt crystals were identified throughout all samples (Figure 2c; Figures S8–S10, Supporting Information). While these findings do not provide the exact binding status of calcium-ions, they are consistent with former studies on according hydrogels, and Ca^{2+}-ions should be coordinated by cellulose hydroxyl groups in-between cellulose molecule chains (as verified by DFT calculations in cited works).[38,39] Based on the finding that all ions are molecularly dispersed, it is now possible to describe the influence of calcium ion content in aerogels on textural properties quantitatively.

Depending on c_{cell}, different mass fractions w_{ca2+} are required to affect the microstructure. At higher cellulose concentrations,

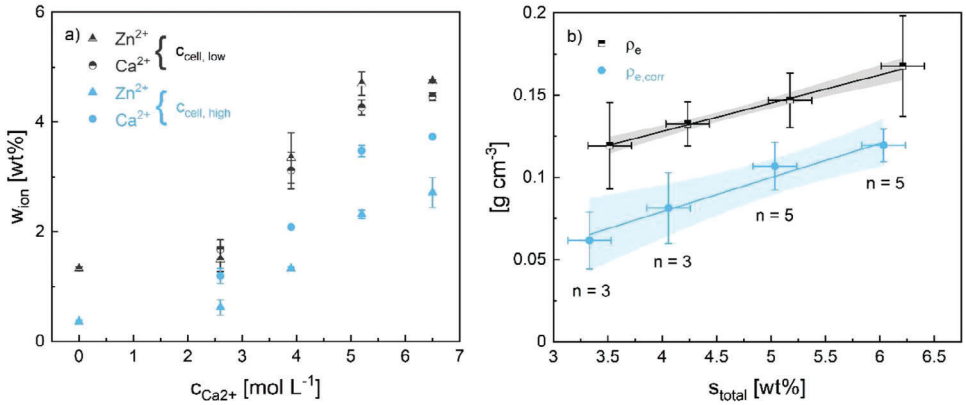

Figure 3. a) Weight content (w_{M2+}) of Ca^{2+} and Zn^{2+} as a function of calcium ion concentration in the gelation bath (c_{Ca2+}). Error bars correspond to the standard deviation of double determinations. b) envelope density of aerogels and total solid content plotted vs. corrected cellulose concentrations. Error bars correspond to standard deviation, straight lines to linear fitting. Hatched areas represent the 95% confidence interval.

a comparably less amount of Ca^{2+} ions is required to create new mesopore volume and to decrease the macropore volume (**Figure** 4a,b). It is interesting to note that V_{meso} reaches similar values at different cellulose concentrations, while V_{macro} is generally lower at $c_{cell,high}$, especially in the low range of w_{Ca2+} where the network formation is mainly driven by non-solvent induced coagulation. This result is consistent with SEM pictures, which show larger macropores at $c_{cell,low}$ as compared to aerogels obtained at $c_{cell, high}$ (Figures S8 and S9, Supporting Information). The mean mesopore diameter is affected in a similar manner: lower mean pore diameters are obtained at $c_{cell,high}$ and less calcium ions regarding cellulose are required to reduce the mesopore size (Figure 4c). At $c_{cell,low}$ and in the range of $w_{Ca2+} \geq 3$ wt.%, an increase of the calcium ion content leads not to a further decrease of $d_{pore, mean}$, indicating that the system runs into a lower limit of $d_{pore,mean} \approx 24$ nm. In contrast, a linear decrease of the mean pore diameter in dependence of entrapped calcium ions down to a minimum of $d_{pore, mean} = 15.3 \pm 0.6$ nm is obtained at $c_{cell,high}$ (Figure 4c). If the overall picture presented in Figure 4a–c) is considered, it seems reasonable to assume that each cross-linking-event with calcium ions is more likely to result in the formation of new mesopore volume if the solid content is higher, resulting therefore in generally denser connected gels with smaller mesopores.

Since textural properties are not independently adjustable and show a complex dependence on ion as well as cellulose content, multiple non-linear regression analysis was used as tool to describe changes covered in the parameter study in a quantitative manner (**Table** 1, for analysis of variances see Table S3, for parameter plots we refer to Figure S11, Supporting Information). Resulting interpolative equations can be used to adjust the microstructure of Zn-Cell based aerogels in a wide range by simple variation of the process parameters c_{Ca2+} and c_{cell} and allows estimation of the Ca^{2+} amount being necessary to create new mesoporous voids. This is especially useful to tune and optimize the aerogels properties for various different applications which might not necessarily be connected to transparency, e.g. as adsorbents, in controlled loading and release or use as soft-template for the production of mesoporous carbon matrices.

Although the models in Table 1 are accurate when used for interpolation, an extrapolation to even higher Ca^{2+}-ions contents give an indication that the pore morphology can be further shifted toward smaller pore sizes. Given that all systems included in the parameter study contained a significant amount of Zn^{2+}-ions, an additional immersion of hydrogels into a fresh Ca^{2+} solution may lead to a further substitution of Zn^{2+}. Additional ion exchange was therefore carried out by immersing hydrogels ($c_{cell} = 5$ wt.%) formed at $c_{Ca2+} = 6.5$ mol L^{-1} two additional times in an aqueous calcium chloride solution of the same concentration prior to further processing. The resulting aerogels contained an increased Ca^{2+}-content ($w_{Ca2+} = 10.1 \pm 0.3$ wt.%), while almost all Zn^{2+}-ions were driven out of the system ($w_{Zn2+} < 0.3 \pm 0.1$ wt.%). A shift of the mesopore size distribution shows, that additional Ca^{2+}-crosslinking leads to smaller mesopores ($d_{pore, mean} = 9.4$ nm, Figure 4d). Pores of according size being formed by tightly entangled nanofibers are also visible in high-resolution SEM pictures (Figure 4e). Images of lower magnification show the homogeneity of the sample and absence of larger pores (Figure 4e). Results of the BET method show a low BET C-Constant ($C = 8.4$) and poor correlation of the BET-plot (Figure S2c, Supporting Information), which may be indicative for the presence of micropores, since the BET-concept is inadequate in mixed meso- to microporous systems.[41,45] The commonly employed methods for evaluation of microporosity in presence of mesopores, including the t-plot, Dubinin-Radushkevic (DR), Dubinin-Astakov and techniques rooted in statistical mechanics (density functional theory) each present unique limitations and assumptions, which depend on the nature of the absorbent surface, the ratio of meso- to micropores as well as on the pores geometry.[41,45,46] Since biopolymer aerogels show commonly macro- to mesoporous pore structures without significant micropores contribution, there are no established standard methods to evaluate the transition to microporous biopolymer aerogels: studies on N_2-physisorption of meso- to microporous systems have so far been focused on other materials (e.g. carbonaceous or silica based). These results are not necessarily transferable to highly polar biopolymer-systems. Yet, in our case, the DR-method shows an appropriate linear correlation (R^2 0.999, inset of Figure 4d) if applied to the same p/p_0 range

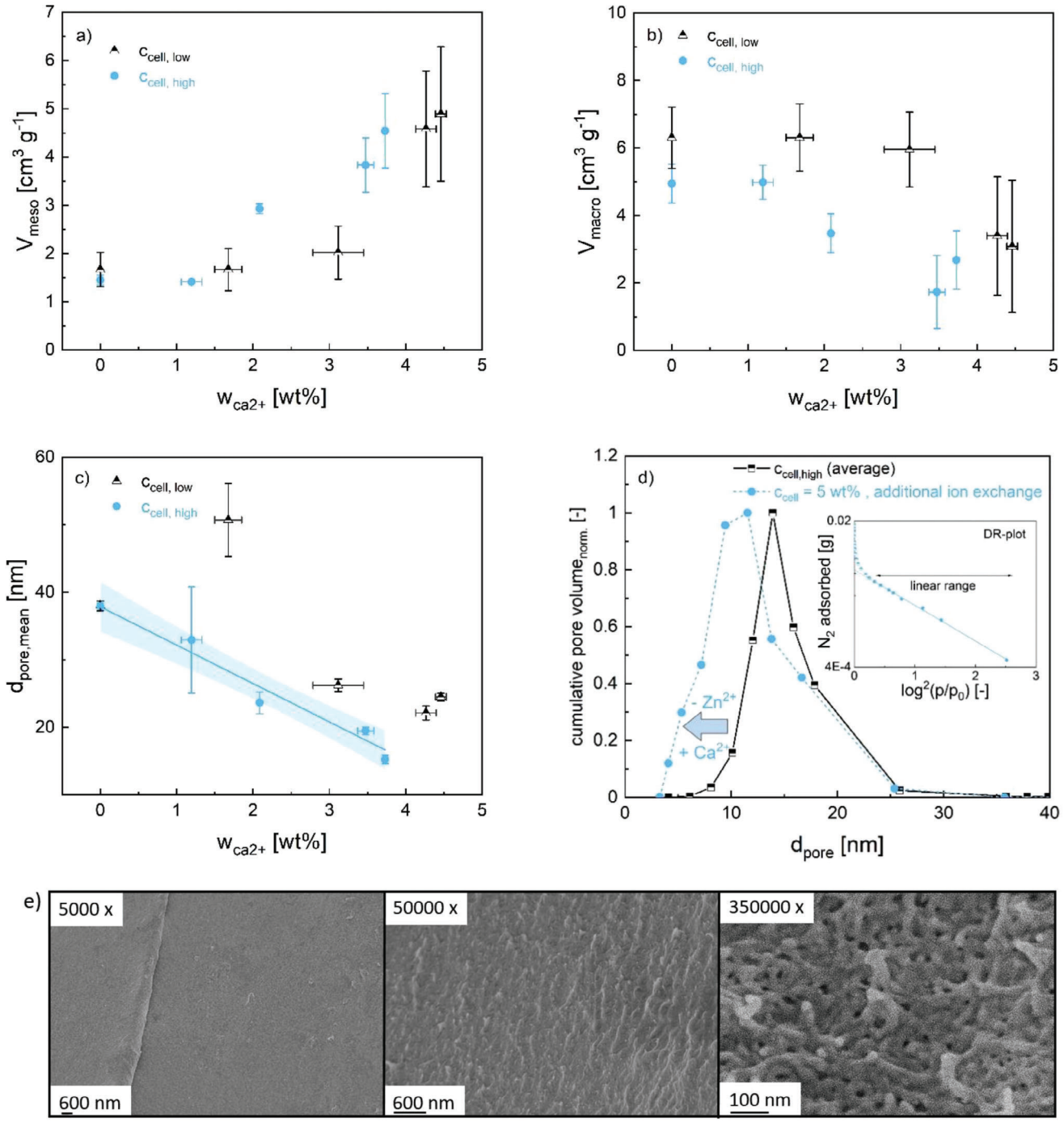

Figure 4. a) Specific pore volume (mesopores), b) macropore volume and c) mean pore diameter (mesopores) for cellulose aerogels, all plotted vs. calcium ion content in aerogels. Error bars correspond to the standard deviation of averaged values at $c_{cell, low}$ and $c_{cell, high}$ ($n = 2$). The straight line gives a linear fit (R^2 0.985), the hatched area represents the 95% confidence interval. d) Mesopore size distribution of cellulose aerogels obtained at $c_{cell,high}$ and c_{Ca2+} = 6.5 mol L^{-1} in comparison to the mesopore size distribution obtained after additional ion exchange from Zn^{2+} to Ca^{2+}. Lines are drawn to guide the eye. The inset shows the Dubinin-Radushkevic plot. e) SEM pictures of aerogel pore structures obtained after additional ion exchange from Zn^{2+} to Ca^{2+}; different magnifications.

Table 1. Predictive equations for calculation of microstructural properties derived from regression analysis. Graphical representations are denoted in Figure S12 (Supporting Information).

Property	Interpolative equation	R^2_{model}	$R^2_{adjusted}$	$R^2_{predicted}$	Std. error[a)] ±
V_{meso} [$cm^3\ g^{-1}$]	$V_{meso} = 1.50 - 0.18 \cdot c_{Ca2+} + 1.71 \cdot c_{ca2+}{}^2$	0.852	0.833	0.783	0.57
V_{macro} [$cm^3\ g^{-1}$]	$V_{macro} = 9.30 - 0.68 \cdot c_{cell} + 3.54 \cdot c_{Ca2+} - 1.55 \cdot c_{cell} \cdot c_{ca2+} - 0.02 \cdot c_{cell}{}^2 - 0.11 \cdot c_{ca2+}{}^2 + 0.17 \cdot c_{cell}{}^2 \cdot c_{ca2+}$	0.922	0.886	0.843	42.6
S_m [$m^2\ g^{-1}$]	$S_m = -221 + 191 \cdot c_{cell} + 15.4 \cdot c_{Ca2+} - 6.77 \cdot c_{cell} \cdot c_{ca2+} - 16.9 \cdot c_{cell}{}^2 + 10.3 \cdot c_{ca2+}{}^2$	0.923	0.896	0.861	0.6
$d_{pore,mean}$ [nm]	$(\sqrt{d_{pore,mean}})^{-1} = 7.45 \cdot 10^{-2} + 1.36 \cdot 10^{-2} \cdot c_{cell} + 1.46 \cdot 10^{-2} \cdot c_{Ca2+}$	0.822	0.800	0.759	5.3

[a)] Standard error of predictions based on the according interpolative equations. Errors have the unit of the predicted property.

(p/p_0 = 0.026 – 0.27) as the BET-plot. This could be attributed to the higher versatility of the DR-method, which accounts not only to the external surface adsorption but for adsorption occurring within micropores as well.[47] While the estimated results ($S_{m,DR}$ = 684 $m^2\ g^{-1}$, micropore volume $V_{micro,DR}$ = 0.24 $cm^3\ g^{-1}$) support the presence of a mixed micro-/mesoporous system and of a significant specific surface area, we emphasize that the applied analytics covers only part of the picture: the overall specific surface area provided by meso- and micropores might be significantly higher than detected.

In summary, additional ion exchange of hydrogels from Zn^{2+} to Ca^{2+} offers a straightforward way to refine the microstructure of cellulose aerogels even further. Such tuneability and accessible properties goes beyond the state of the art as well as compared to alternative production routes using different solvents or cellulose regeneration methods.[12,34,35,42]

2.2. Analysis of Light Transmittance

Different textural properties described in section 2.1 result in changes of optical appearance of hydrogels and aerogels (**Figures 5**, S13). Predominantly mesoporous structures of gels obtained at c_{Ca2+} = 5.2–6.5 mol L^{-1} (pore structure II) and c_{cell} = 3.25–5.00 wt.% allow light to pass through both hydro- and aerogels. Aerogel discs with homogeneous appearance were only obtained at the highest calcium ion concentration (c_{Ca2+} = 6.5 mol L^{-1}), while those produced at c_{Ca2+} = 5.2 mol L^{-1} contained inhomogeneities in some cases. Aerogels produced at the highest solid content (c_{cell} = 6.00 wt.%) deviate from this general trend by showing opaque (c_{Ca2+} = 5.2 mol L^{-1}, d ≥ 1.5 mm) or slight inhomogeneous (c_{Ca2+} = 6.5 mol L^{-1}) appearances (Figure S13, Supporting Information).

UV–vis transmission spectra of cellulose aerogels (**Figure 6a**; Figure S4, Supporting Information) reveal a strong relation between λ and the total transmission, whereas generally higher transmissions are being obtained for substrates produced at c_{Ca2+} = 6.5 mol L^{-1} as compared to c_{Ca2+} = 5.2 mol L^{-1}. A similar trend is detected for the UV-cutoff wavelength (λ at T ≤ 0.1%), which is shifted accordingly from the range of ≈ 305 – 405 nm (c_{Ca2+} = 5.2 mol L^{-1}) to lower wavelengths of 225 – 305 nm (c_{Ca2+} = 6.5 mol L^{-1}) in dependence of c_{Ca2+}. Since the transparent samples exhibit low densities and nearly identical material composition (see Figure 3a, variation in calcium ion content among transparent samples is at most ± 1 wt.%), we suggest that the

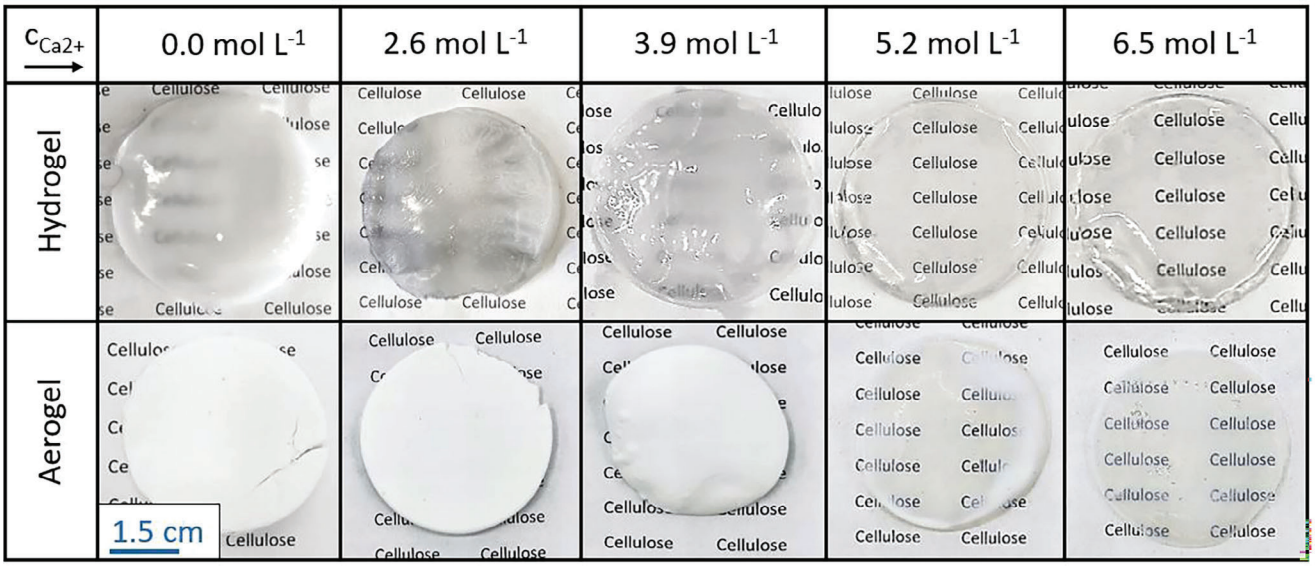

Figure 5. Images of hydrogels and aerogels (d = 1.5 mm) obtained at c_{cell} = 5 wt.% at different concentrations of calcium ions in the gelation bath.

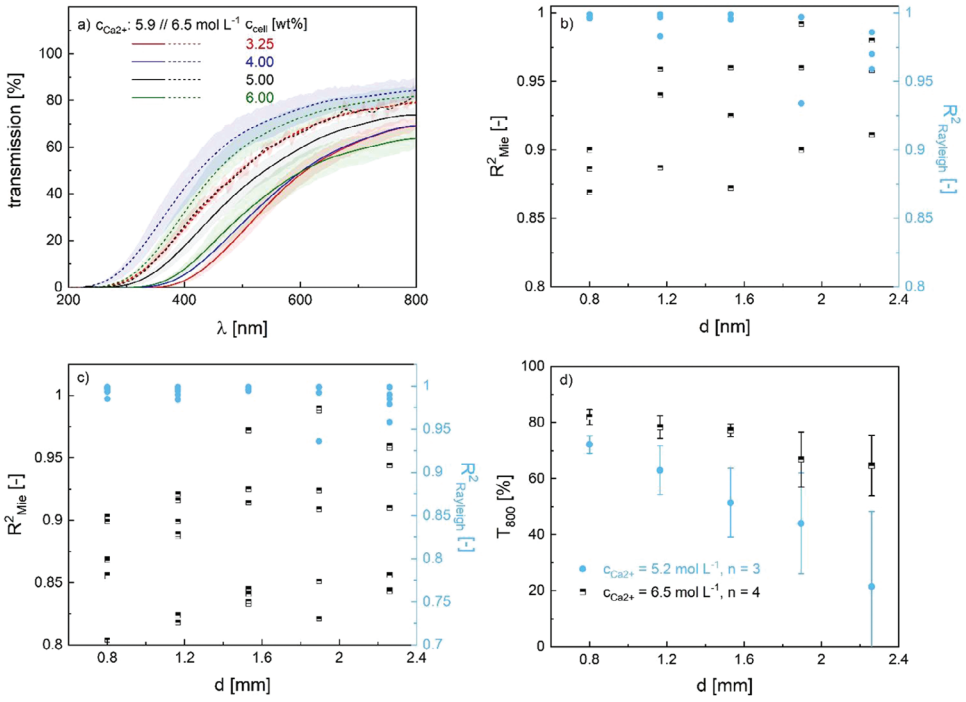

Figure 6. a) UV–vis transmission spectra obtained at different levels of c_{Ca2+} and c_{cell} at a constant substrate thickness of d = 0.8 mm. Highlighted areas correspond to the standard deviation of the average value ($n = 3$). b,c) Correlation coefficients $R^2_{Rayleigh}$ and R^2_{Mie} in dependence of substrate thickness at different values of c_{Ca2+} (according fits are represented in Figures S14 and S15, Supporting Information). d) Transmission at a wavelength of 800 nm in dependence of c_{Ca2+} and d. Values are averaged across different levels of c_{cell}, error bars correspond to the standard deviation of the average.

differences in transmission are primarily rooted in scattering effects caused by the interaction of light with the aerogel microstructure, while differences in absorption behavior of the solid matrix should be negligible.[48] In case of scatterers dimensions being similar to the incident lights wavelength, the Mie's theory describes the dependence of the scattering coefficient and transmitted light intensity. In this case, the scattering intensity varies with the first power of the inverse wavelength (Mie-scattering), as has e.g. been shown for porous silicons and transparent polyisocyanurate – polyurethane aerogels.[49] In case of negligible absorption, smaller scatter sizes (≈1/10 of λ) and little multiple scattering, the transmission behavior of aerogels can be described via Rayleigh scattering theory:

$$T = A \cdot e^{\left(\frac{Bd}{\lambda^4}\right)} \quad (5)$$

with T being the transmission, A being a constant related to surface defects, B being the wavelength dependency coefficient and d the substrates thickness.[48–50] According to the relations described above, fundamental insights about the dominant scattering mechanism can be elucidated from the shape of the transmission curves by linear fitting of d/λ^4 and d/λ vs. -ln(T) (Figures S14 and S15, Supporting Information). Hereby, comparison of respective correlation coefficients ($R^2_{Rayleigh}$ and R^2_{Mie}) provides an indication about the dominating scattering mechanism.[49] For substrates produced at $c_{Ca2+} = 5.2$ mol L^{-1}, a clear assignment of the dominant scattering mechanism was not always possible for large thicknesses (Figure 6b). In all other cases, the wavelength-dependency of transmission can accurately be described by d/λ^4 vs. –ln(T) ($R^2_{Rayleigh} > 0.98$, Figure 6b,c), showing that mainly Rayleigh scattering occurs.

In order to quantify the impact of the substrate thickness d on light transmission across different levels of c_{Ca2+}, transmission values were compared at a constant wavelength of $\lambda = 800$ nm (T_{800}). General trends in dependence of c_{Ca2+} and d are displayed in Figure 6d), wherein each individual data point represents a mean value throughout all levels of c_{cell}. For substrates produced at $c_{Ca2+} = 5.2$ mol L^{-1}, the total transmission covers a wide range (T_{800} = 3%–76%) with a significant reduction as the substrate thickness increases. This trend is significantly less pronounced if a higher concentration of calcium ions in the regeneration bath is used ($c_{Ca2+} = 6.5$ mol L^{-1}), and transmission values of up to $T_{800} = 76\%$ can still be achieved at max. d = 2.3 mm. We suggest that these results are partly rooted in the production procedure, whereas the upper part of the Zn-Cell sol is initially subjected to a high concentration of Ca^{2+}-ions, while the bottom one is not. Phase separation between Zn^{2+}- rich molten salt hydrate and water can be assumed to occur generally quickly due to the high concentration gradients (leading to a high driving force) and low viscosity of the gelation solution.[22] Since Ca^{2+}-ions are consumed during their diffusion through the gel matrix, a Ca^{2+}-gradient is formed in the gel, resulting in water-rich and Ca^{2+}-lean zones. Consequently, a non-homogeneous gel body is formed, which contributes to Mie-scattering as confirmed by scattering analysis of the thicker discs (Figure 6b,c). This assumption agrees with former works, where a slow, reversible reordering of cellulose chains in the center of Zn-Cell hydrogel monoliths during the ion

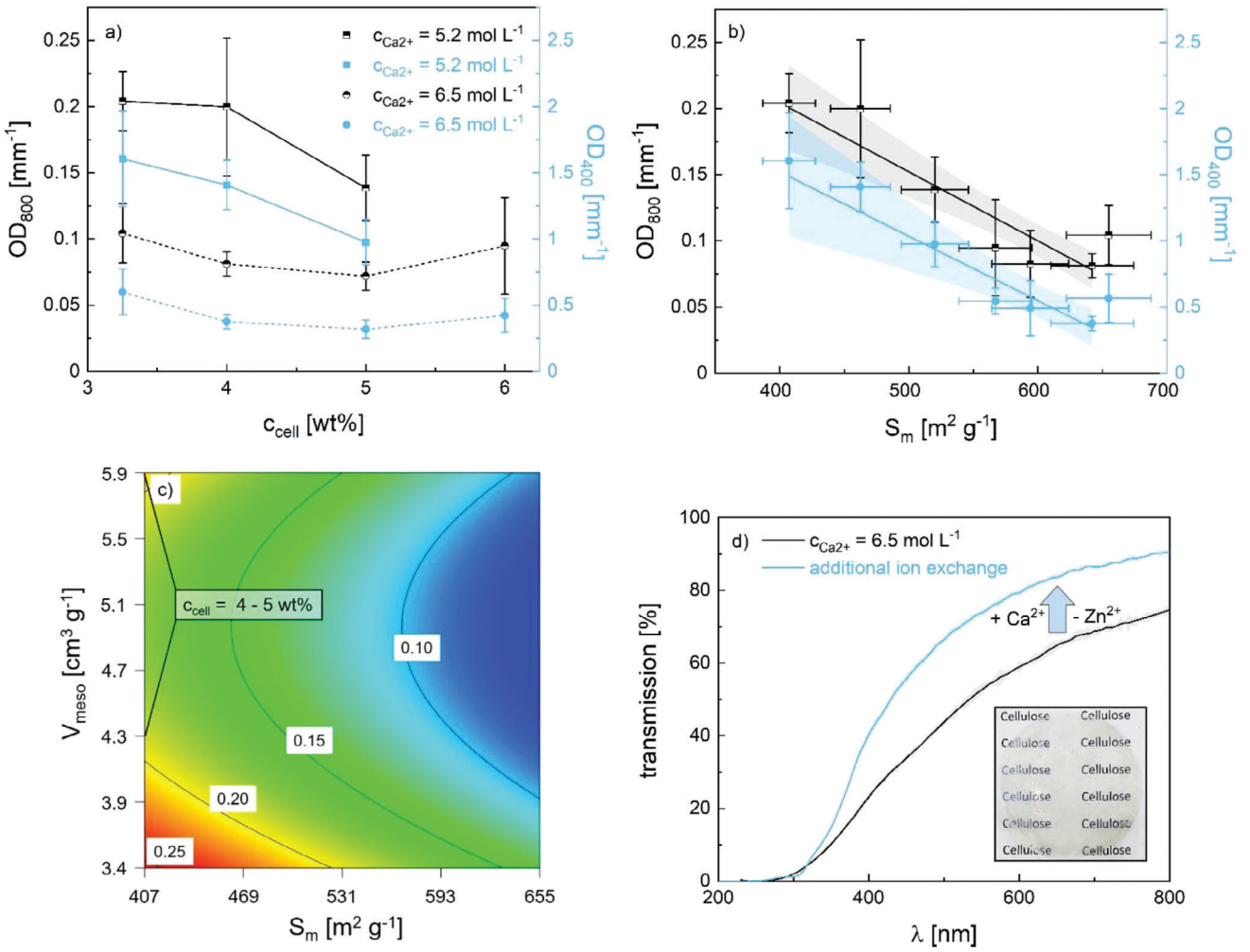

Figure 7. a) Optical density in dependence of c_{cell} at different levels of c_{Ca2+}. Values are averaged across all tested substrate thicknesses d, error bars correspond to the standard deviation ($n = 5$). Lines are drawn to guide the eye. b) Optical density in dependence of the specific surface area. Values are averaged for all tested substrate thicknesses d, y-error bars correspond to the standard deviation of the averaged values ($n = 5$). The x-error bars correspond to the standard error of the BET-method. Lines represent linear fits, highlighted areas the 95% confidence interval. c) Contour plot of the optical density in dependence of S_m and V_{meso}. Inset number represent the values of OD_{800}. d) UV–vis transmission spectra of cellulose aerogels obtained at $c_{cell,high}$ and c_{Ca2+} = 6.5 mol L^{-1} and d = 1.5 mm in comparison to transmission spectra obtained after additional ion exchange from Zn^{2+} to Ca^{2+} (sample shown in inset). Highlighted areas correspond to the standard deviation of the average value ($n = 3$).

exchange from Zn^{2+} to Ca^{2+} (and vice versa) was experimentally visualized over the course of several hours.[38] The influence of process parameters and microstructural properties on light transmission for substrates with different thickness can be assessed by comparing the apparent optical density per mm substrate thickness (OD). Hereby, relationships were analyzed at two different wavelengths of the incident light, λ = 400 nm (OD_{400}) and λ = 800 nm (OD_{800}).

Trends of OD_{800} and OD_{400} follow generally the same course in dependence of process parameters, the latter showing in average six times higher values (**Figure 7a**). Low values of OD_{800} < 0.1 mm^{-1} are only achieved at max. c_{Ca2+} = 6.5 mol L^{-1}, and gels produced at c_{cell} = 5 wt.% show a minimum of the OD. While the presented data is important from an application point of view, it is also of interest to elucidate how aerogels microstructural properties are connected to the OD. Owing the complex nature and diversity of different aerogel pore networks, such relations are expected to depend individually on specific materials and type of building blocks being responsible for light scattering. As a result, various textural parameters have been documented as being linked to the scattering properties of aerogels in the past, such as the nanoparticle size (in case of colloidal systems),[2,49] pore size,[51–53] envelope density[2,16] and specific surface area.[52] Since the mean mesopore diameters of transparent substrates in this work are rather small ($d_{mean} \leq 24$ nm) and below the range where pores could significantly contribute to light scattering, no relation between d_{mean} and the OD was found. Nevertheless, most substrates contained also pores which exceed the d_{mean}, as evidenced by the results from BJH and SEM analysis (Figure 2d,e; Figures S7–S10, Supporting Information). Such larger structural features – even if small in number – should contribute disproportionately high to light attenuation, since the scatterers diameter is

related by the power of six to the scattering intensity in Rayleigh scattering.[49] Interestingly, the specific surface area shows a linear relation with the OD in the range of pronounced changes (Figure 7b). However, interpretations about the influence of individual structural parameters are not possible, since the specific surface area might be influenced by a variety of microstructural changes (like e.g. presence of larger mesopores, small macropores and variation of cellulose fiber thickness) which are not independently adjustable. A refined description is provided via regression analysis (Figure 7c, for ANOVA see Table S4, Figure S16, Supporting Information), which allows estimation of the OD_{800} (standard deviation ± 0.025 mm^{-1}) by taking also the influence of the mesopore volume into account, Equation (6).

$$OD_{800}[mm^{-1}] = 1.23 - -4.7 \cdot 10^{-4} \cdot S_m - -0.35 \cdot V_{meso} + 3.6 \cdot 10^{-2} \cdot {V_{meso}}^2 \quad (6)$$

In order to minimize possible influences of mass-transport during gelation, only results from thin substrates (d = 0.8 – 1.2 mm) were included in the analysis. The relation between BET/BJH and UV–vis data described via Equation 6 is consistent with the minimum of the OD detected at c_{cell} = 5.00 wt.% (Figure 7a). We surmise, that both quantities S_m and V_{meso} are good measures for the fineness of the pore network: e.g. an increase in V_{meso} is accompanied be the loss of macropores (see Figure 2b) and therefore of larger building blocks, resulting in mitigation of scattering. Notably, Equation 6 is only valid for mainly mesoporous systems (pore structure II) which were included in the parameter study and contain both Ca^{2+} and Zn^{2+} ions.

Taking mass transport and homogeneity of the systems into account, it is reasonable to assume that an additional ion exchange from Zn^{2+} to Ca^{2+} after the hydrogelation step should result in further enhancement of light transmission. The according substrates show indeed significantly improved optical properties as reflected by an increase of T_{800} = 75% to T_{800} = 91% (d = 1.5 mm) and higher transmission in the range of λ = 320 – 800 nm (Figure 7d). Since the pore structure is composed of even smaller building blocks after complete ion exchange to Ca^{2+}, resulting substrates show the by far highest transmission, which converts to low values of OD_{400} = 0.25 and OD_{800} = 0.03 mm^{-1}.

2.2.1. Thermal and Mechanical Properties

Additional application-relevant properties of cellulose aerogels like mechanical toughness and thermal conductivity were evaluated for selected samples. The thermal conductivity κ was assessed at 10 °C for the sample with the highest mesopore volume (see Figure 1a,b) and best optical properties in the parameter study (c_{cell} = 5 wt.%, c_{Ca2+} = 6.5 mol L^{-1}), using a FOX 200 heat flow meter according to ASTM C518 and ISO 8301 standards. The thermal conductivity (κ = 0.047 W m^{-1} K^{-1}) is rather high as compared to other cellulose and other bio-aerogels with most reported values in the range of ≈ 0.016 – 0.030 W m^{-1} K^{-1},[54] however to the best of our knowledge this is the first reported thermal conductivity value of the cellulose aerogel prepared via extensive Ca^{2+}-cross-linking.[12] One possible reason for the comparatively high thermal conductivity might be the inclusion of significant amounts of metal ions in the aerogel matrix. Yet our results clearly show that reducing the ion content is not possible without compromising the optical properties. We would also like to emphasize that the current cellulose aerogel formulation is highly hydrophilic and in its present form would need a hydrophobization step before being suitable in any thermal insulation application of aerogels such as window glazing among others. In mechanical testing via uniaxial compression tests (c_{cell} = 5.0 wt.%), samples exhibited elastic-plastic deformation behavior without any fracture occurrence in the investigated range up to a compressive strain of 80% (Figure S17, Supporting Information). The applied force led to irreversible deformation, and no recovery of the aerogel shape was observed after compression. Typical stress-strain curves as reported for porous materials present generally three phases (1. linear elastic range 2. plateau, regime of pore collapse, 3. densification) all of which are also commonly observed in compression of cellulose aerogels.[12,22,24,27–29,55] In our case, these phases were only observed for the sample produced at the highest calcium ion content (c_{Ca2+} = 6.5 mol L^{-1}). The Young´s modulus E was determined accordingly in the linear elastic range via regression. As compared to mechanical weak samples coagulated in pure water (E = 0.1 MPa) an increase of c_{Ca2+} to 5.2 mol L^{-1} (E = 7.8 MPa) and 6.5 mol L^{-1} (E = 22.7 MPa) resulted in a remarkable improvement of the gels mechanical stability. While aerogels Young´s moduli are generally expected to scale with the density in form of a power law ($E \approx \rho_e^n$ with n being related to the choice of material)[55] our findings for different samples of the same density and different Ca^{2+}-content (see Table S2, Supporting Information) show, that the increase of Ca^{2+} leads to changes of the bulk materials strength. These changes and the loss of large pores at high c_{Ca2+} are most likely the decisive factors for the increase of E at constant ρ_e in our case. In case of high Ca^{2+}-cross-linking, Young´s moduli obtained in this work fit well within the range of other Zn-Cell-derived cellulose aerogels and exceed e.g. the values reported for cellulose aerogels from calcium thiocyanate based molten salt hydrates (E ≈ 2 – 10 MPa) and the typical range of silica aerogels with comparable density (E ≈ 1 – 3 MPa).[12,34,35,56] Given the distinct advantages, disadvantages and limitations of different production routes it is interesting to compare the materials produced in this study based on application-relevant properties (such as maximum thickness, specific surface area, thermal conductivity, and light transmittance) as well as production process-related criteria (use of oxidants, pretreatment methods, and cellulose solvents) with the current representative research in the field (**Table 2**). Hereby only "pure" cellulose aerogels are considered, and hybrid materials such as cellulose/silica mixtures or nanoparticle containing materials are not considered.

In order to make light transmittance comparable across different studies, the OD_{800} was estimated from reported transmittance and thickness values. Fundamentally, we can distinguish between molecular, and CNF based production routes. In the CNF approach, chemical cellulose modification and supercritical drying are required in order to achieve a combination of favorable properties (low optical density, high specific surface area, sufficient thickness of products and thermal conductivity below that of air). The generally lower thermal conductivities of aerogels obtained by the CNF-route might be rooted in the limited heat transfer via the thin CNF-backbone. While high

Table 2. Summary of representative research on transparent, non-hybrid cellulose aerogels and selected properties and production approaches. If available, the maximum values of S_m and d obtained in respective studies are provided; for κ and OD_{800}, the minimum values are presented.

Approach	Chemical pre-treatment	Cellulose solvent	D [mm]	OD_{800} [mm^{-1}]	S_m [$m^2\ g^{-1}$]	κ [$W\ m^{-1}\ K^{-1}$]	Refs.
molecular	none	$ZnCl_2/H_2O$	2.3	0.03	684	0.047	this work
molecular	none	AMIMCl	4.0	0.05	227	0.033	[22]
molecular	none	AMIMCl	3.0	0.04	206	n.d.	[23]
molecular	none	Trifluoroacetic acid	1.0	0.04	492	0.024	[24]
molecular	none	LiOH or NaOH/Urea/H_2O	n.d.	n.d.[b]	404[b]	n.d.	[25,26]
CNF	TEMPO + $NaClO_2$ oxidation	–	1.0	0.03	600	0.018	[28]
CNF	2-step oxidation ($NaIO_4$ + $NaClO_2$)	–	1.0	0.09	588	0.018	[29]
CNF	repetative oxidation (TEMPO + NaOCl + NaBr)	–	2.5	< 0.01	401	0.015	[30]
CNF[a]	none	–	< 0.03	> 1.50	208	n.d.	[31]
CNF[a]	fluorination via Perfluorodecyl-triethoxysilane	–	≤ 0.2	0.53	96	0.033	[32]

[a] Products obtained via ambient drying. All others work: use of supercritical CO_2 drying; [b] Thickness of dried samples is not given, estimation of OD_{800} therefore not possible. Production was started from 0.5 mm thick cellulose solution layer. S_m of sample provided for sample reported in[27] (transmittance ≈78% at λ = 800 nm).

performance materials are obtainable in the CNF-route (see Abraham et al.),[30] environmental aspects and costs of oxidants and cellulose pre-treatment have to be considered: in particular, TEMPO-mediated oxidation could pose a significant obstacle to large-scale implementation.[57] In contrast, cellulose oxidation can be avoided in molecular approaches, but products with generally higher thermal conductivities (approx. equal or above that of air) are obtained. Hereby, the Zn-Cell route leads to highly competitive materials in terms of optical properties and to date highest reported S_m while promoting overall sustainability and lowering of production costs due to the choice of an aqueous, salt based cellulose solvent.

3. Conclusions

In this work, we present for the first time a purely salt induced route toward transparent cellulose aerogels by crosslinking of cellulose molecule chains with calcium ions via ion exchange from Zn^{2+} to Ca^{2+}. Such approach facilitates a high degree of structural control in cellulose aerogels, allowing to tailor properties like the specific surface area, mesopore size and ratio of macro- to mesopores as well as mechanical properties in a wide range. Mainly mesoporous, ordered pore networks (pore structure II) are not common for cellulose aerogels, which show in most cases a multiscale porosity, including macropores. The absence of larger structural features for highly crosslinked products allows light to pass through the aerogel-matrix, which is not possible for aerogels produced with coagulative methods. From a processing point of view, the use of expensive or non-green solvents is not necessary, and microcrystalline cellulose can be used without pretreatment (e.g. oxidation). Scalability of the production process is principally given, since excess salts can be recovered using industrially available standard methods. One challenge lies in the high hydrophilicity of the products, rendering them sensitive against liquid water and vapor. The latter leads to a quick loss of properties, e.g., when substrates are stored under open air. While mitigation of this effect can be achieved by complete exchange of Zn^{2+} by Ca^{2+}, quality-preserving post-modification methods (e.g. silanization) for hydrophobization of transparent cellulose aerogels have already been established and should also being applicable for systems produced in this study.[30] Our results showed that formation of macropores is suppressed in presence of sufficient Ca^{2+}-amounts during gelation: an effective and fast Ca^{2+}-mass-transport in the gelling system is therefore the key to homogeneous and transparent substrates. While one limiting factor of this attempt is the mass transport of Ca^{2+} during gelation, subsequent ion exchange in the hydrogel state (after the first gelation step) represents an additional possibility to complete the Ca^{2+}-crosslinking. This two-step method leads to aerogels with maximized light transmission and smallest mesopores. It is also expected that the range of accessible substrate thicknesses can be broadened, if additional ion exchange in hydrogel state is applied. Results of this study suggest, that Ca^{2+}-crosslinking of dissolved cellulose or of pre-formed cellulose hydrogels is a so far unexploited, simple way toward enhanced microstructural design of cellulose aerogels. The high degree of structural control makes Ca^{2+}-cross-linked cellulose aerogels suitable for various applications, particularly where pore size and surface area are crucial (such as controlled loading and release, separation processes and e.g. use as transparent membranes). In contrast, their thermal conductivity has to be further optimized for thermal insulation applications. While this proof-of-concept study opens up a new pathway toward cellulose aerogels, the limits of the Ca^{2+}-crosslinking approach have still to be assessed: further variation of material properties might be achieved by introduction of other coordinating metal ions/ion mixtures (e.g. Al^{3+} or Cu^{2+}), change of the used salt hydrate for cellulose

dissolution or use of cellulose with different molecular chain lengths.

4. Experimental Section

Preparation of Zn-Cellulose Stock Solutions: In a first step, cellulose pastes were prepared by mixing of 2.4–4.9 g microcrystalline cellulose type II powder (JRS Pharma GmbH & Co. KG, Vivapure®, 101) with double weight amount + 6.0 g of demineralized water. Aqueous $ZnCl_2$ as cellulose solvent was prepared by adding 48.7 g $ZnCl_2$ (crystalline powder, purity ≥ 97 wt.%, Carl Roth GmbH & Co. KG) to 12.0 g demineralized water and stirring the mixture at 65 °C for 30 min. The cellulose pastes were added to $ZnCl_2$-solutions after a swelling time of 30 min, followed by mixing for additional 30 min (T = 65 °C). The resulting colorless, transparent aqueous $ZnCl_2$-Cellulose solutions (Zn-Cell) with different overall cellulose content c_{cell} regarding the overall mass (c_{Cell} = 3.25–6.00 wt.%) were stored in a sealed glass bottle for an additional hour without stirring at 65 °C to remove gas bubbles and were subsequently used for hydrogel formation.

Preparation of Hydrogels: Gelation solutions were prepared by dissolving different amounts of calcium chloride dihydrate (Carl Roth GmbH & Co. KG) in demineralized water. The concentration of calcium chloride (c_{Ca2+}) was varied in the range of c_{Ca2+} = 0 – 6.5 mol L^{-1}. For production of hydrogel slabs, Zn-Cell sol (1.3 – 3.6 mL) was preheated to 65 °C and transferred into glass petri dishes (inner diameter 52.2 mm, height 15.1 mm). Zn-Cell filled petri dishes were directly immersed into cups, filled with 100 mL of preheated (70 °C) gelation solution, sealed and stored at a temperature of 70 °C for 2 h. Afterwards, the gelation solution was discarded, and the obtained hydrogel slabs were transferred to solvent exchange without further washing.

Solvent Exchange: Hydrogels were subjected to a direct solvent exchange, without extra washing steps, by immersing the substrates in 100 mL of 99.9 wt.% anhydrous ethanol (EtOH, Carl Roth GmbH & Co. KG) and storing at room temperature for 24 h. Subsequently, a second solvent exchange step was carried out by replacing EtOH with 50 mL of fresh anhydrous EtOH. After a minimum final ethanol concentration of 98.0 wt.% was achieved in the liquid phase (controlled via density measurements, Anton Paar, DMA 4500 M), alcogels were sealed into filter paper bags, covered with a small amount of fresh EtOH and stored till supercritical drying.

Supercritical Drying: Alcogels were transferred in sealed filter paper bags into a high-pressure autoclave with an overall volume of 3.9 L for supercritical drying. The supercritical drying was performed at a temperature of 40 °C and pressure of 110 bar under a continuous flow of CO_2 (flow rate = 80–100 g min^{-1}) for 4 h. Aerogel substrates were collected after slow depressurization (1 bar min^{-1}) of the autoclave and stored in sealed, CO_2-filled cups (SecurTainer™ III, Thermo Fisher Scientific) in a desiccator prior to analysis.

Characterization: Volumetric shrinkage ΔV [%] of slabs was obtained by determining the diameter and thickness with a caliper (double determination). Hereby, volumetric shrinkage from hydro- to alcogel after complete solvent exchange ΔV_{alco} as well as from hydro- to aerogel ΔV_{aero} were determined. The envelope density ρ_e of aerogel slabs was calculated from the samples weight (model balance: Precisa S520, Precisa Gravimetrics AG) and volume:

$$\rho_e = \frac{m}{V} \tag{7}$$

with m being the sample weight and V the sample volume. Density determinations were carried out in duplicate. In order to set distinct aerogel substrate thicknesses d, different amounts of Zn-Cell sol were used in the production process and d was determined after the supercritical drying step. The relative error on d (± 3.4%) was estimated based on the slope of a linear calibration fit (data and method: Figure S1, Supporting Information). The skeletal density ρ_s was determined via helium pycnometry (Multivolume Micromeritics 1305, 6-fold measurement) at room temperature. The overall porosity ϵ was estimated from envelope and skeletal densities:

$$\epsilon = \left(1 - \frac{\rho_e}{\rho_s}\right) \cdot 100\% \tag{8}$$

Low temperature N_2 adsorption–desorption analysis was used (Nova 3000e Surface Area Analyzer, Quantachrome Instruments) to determine the mass specific surface area (S_m), mesopore size distribution, and mesopore volume (V_{meso}) of aerogels. An overall sample mass of ≈20 mg was used for each analysis. Samples were degassed under vacuum at a temperature of 60 °C for 4 h prior to analysis. S_m was estimated using the BET (Brunauer–Emmett–Teller) method based on highly correlated linear fitting of the BET model (Figure S2, Supporting Information), p/p_0 range = 0.027–0.27, $R^2 \geq 0.9998$) derived from Type IV N_2 adsorption isotherms (Figure S3, Supporting Information). V_{meso} and the mean mesopore diameter ($d_{pore,\ mean}$) were estimated via the BJH (Barrett–Joyner–Halenda) method. Standard errors of S_m ± 20 $m^2\ g^{-1}$ and of V_{meso} ± 0.6 $cm^3\ g^{-1}$ were estimated based on a threefold determination. The inner pore structure of aerogels was characterized via scanning electron microscopy (SEM, Zeiss Supra VP55, Jena, Germany). Substrates were cut open with a razor blade and sputtered with a conductive, thin (≈6 nm) layer of gold (Sputter Coater SCD 050, BAL-TEC) prior to analysis. Measurements were carried out under high vacuum at an accelerating voltage of 3.00 kV, a working distance of 2.9–4.0 mm using an in-lens detector. Photographs of substrates were taken in a fotobox. Brightness and contrast of the SEM images and photographs were optimized using PowerPoint 2016. The Ca- and Zn-content of aerogels (≈20 mg of sample each) was determined using an ICP-OES (AVIO 550; Perkin Elmer) via external calibration against standards with known concentrations of Ca and Zn. All analyses were carried out as double determinations and checked for accuracy by quality control standards with known certified concentrations. Initial digestion of samples was achieved via acidic digestion (3 ml HNO_3,1 ml H_2O_2) using a Microwave system (Microwave 7000, Anton Paar) at 280 °C. Transmission spectra (Figure S4, Supporting Information) of aerogel slabs were recorded by placing substrates of a thickness between d = 0.8 – 2.3 mm vertically in the beam of a UV–vis spectrometer (Evolution 300 UV, ThermoFisher Scientific) equipped with a xenon lamp. The wavelength of the incidents light λ was varied between λ = 200–800 nm. The apparent optical densities per millimeter substrate thickness (OD) were calculated from the transmission values at two distinct wavelengths of the incident light (OD_{400} and OD_{800} at λ = 400 and 800 nm, respectively) divided by the substrates thickness. Therefore, possible effects of surface reflection were neglected. Taking all experimental variation into account, the relative error of OD on individual measurements (Table S1, Supporting Information) varies in a rather broad range (relative error in average ± 27% for OD_{400} and ± 6% for OD_{800}) translating to ≈ ± 0.008 mm^{-1} (OD_{800}) and ± 0.31 mm^{-1} (OD_{400}). Uniaxial compression tests were carried out using a TA.XTplusC Texture Analyzer from Stable Micro Systems. Cellulose aerogel samples with a thickness of 2.5 – 5.0 mm were compressed with a piston of 4 mm diameter and under constant compression speed (0.15 s mm^{-1}) until a compressive strain of 80% was reached (load cell 500 N). Two specimens were measured for each sample.

Statistical Analysis: The statistical analysis of experimental data was carried out by using Design-Expert statistics software (Version 22.0.6, Statcon, Germany). One-way analysis of variance (ANOVA) was performed to determine if differences between sample means were significant at a significance level of $p < 0.05$.

Supporting Information

Supporting Information is available from the Wiley Online Library or from the author.

Acknowledgements

The authors wish to acknowledge support for this research received from the AERoGELS COST Action CA 18125. The authors acknowledge support from the central laboratory of Hamburg University of Technology for performing elemental analysis.

Open access funding enabled and organized by Projekt DEAL.

Conflict of Interest

The authors declare no conflict of interest.

Author Contributions

The manuscript was written through contributions of all authors. All authors have given approval to the final version of the manuscript.

Data Availability Statement

The data that support the findings of this study are available in the supplementary material of this article.

Keywords

aerogels, cellulose, pore structure, supercritical drying, transparency

Received: May 3, 2024
Revised: August 7, 2024
Published online:

[1] F. Gomollón-Bel, *Chem. Int.* **2022**, *43*, 4.
[2] L. Zhao, E. Strobach, B. Bhatia, S. Yang, A. Leroy, L. Zhang, E. N. Wang, *Opt. Express* **2019**, *27*, A39.
[3] H. Maleki, L. Durães, A. Portugal, *J. Non. Cryst. Solids* **2014**, *385*, 55.
[4] J. Wang, D. Petit, S. Ren, *Nanoscale Adv.* **2020**, *2*, 5504.
[5] T. Linhares, M. T. Pessoa De Amorim, L. Durães, *J. Mater. Chem. A* **2019**, *7*, 22768.
[6] R. Chandrasekaran, M. Hillgärtner, K. Ganesan, B. Milow, M. Itskov, A. Rege, *Sci. Rep.* **2021**,*11*, 10198.
[7] S. Zhao, W. J. Malfait, N. Guerrero-Alburquerque, M. M. Koebel, G. Nyström, *Angew. Chemie – Int. Ed.* **2018**, *57*, 7580.
[8] Q. Liu, A. W. Frazier, X. Zhao, J. A. De La Cruz, A. J. Hess, R. Yang, I. I. Smalyukh, *Nano Energy* **2018**, *48*, 266.
[9] D. J. Lockwood in *Encyclopedia of Color Science and Technology* (Eds: M. R. Luo), Springer, New York, NY **2016**.
[10] S. Takeshita, S. Zhao, W. J. Malfait, M. M. Koebel, *Angew. Chemie – Int. Ed.* **2021**, *60*, 9828.
[11] M. Reimer, C. Zollfrank, *Adv. Energy Mater.* **2021**, *11*, 2003866.
[12] T. Budtova, *Cellulose* **2019**, *25*, 81.
[13] V. G. Parale, K. Y. Lee, H. H. Park, *J. Korean Ceram. Soc.* **2017**, *54*, 184.
[14] R. Subrahmanyam, P. Gurikov, P. Dieringer, M. Sun, I. Smirnova, *Gels* **2015**, *1*, 291.
[15] C. A. García-González, M. Alnaief, I. Smirnova, *Carbohydr. Polym.* **2011**, *86*, 1425.
[16] S. Takeshita, S. Yoda, *Chem. Mater.* **2015**, *27*, 7569.
[17] S. Takeshita, A. Konishi, Y. Takebayashi, S. Yoda, K. Otake, *Biomacromolecules* **2017**, *18*, 2172.
[18] S. Takeshita, S. Zhao, W. J. Malfait, *Carbohydr. Polym.* **2021**, *251*,117089.
[19] F. Liebner, N. Pircher, C. Schimper, E. Haimer, in *Consise Encyclopedia of Biomedical Polymers and Polymeric Biomaterials* (Eds: M. Mishra), CRC Press, Boca Raton, Florida **2017**, Ch. 2.
[20] F. Liebner, A. Potthast, T. Rosenau, E. Haimer, M. Wendland, *Holzforschung* **2008**, *62*, 129.
[21] A. Zaman, F. Huang, M. Jiang, W. Wei, Z. Zhou, *Energy Built Environ.* **2020**, *1*, 60.
[22] Q. Y. Mi, S. R. Ma, J. Yu, J. S. He, J. Zhang, *ACS Sustainable Chem. Eng.* **2016**, *4*, 656.
[23] B. Yuan, J. Zhang, Q. Mi, J. Yu, R. Song, J. Zhang, *ACS Sustainable Chem. Eng.* **2017**, *5*, 11117.
[24] F. Ayadi, B. Martín-García, M. Colombo, A. Polovitsyn, A. Scarpellini, L. Ceseracciu, I. Moreels, A. Athanassiou, *Carbohydr. Polym.* **2016**, *149*, 217.
[25] J. Cai, S. Kimura, M. Wada, S. Kuga, L. Zhang, *ChemSusChem* **2008**, *1*, 149.
[26] J. Cai, S. Kimura, M. Wada, S. Kuga, *Biomacromolecules* **2009**, *10*, 87.
[27] S. Quraishi, S. F. Plappert, T. Grießer, W. Gindl-Altmutter, F. W. Liebner, *Cellulose* **2019**, *26*, 7781.
[28] Y. Kobayashi, T. Saito, A. Isogai, *Angew. Chem., Int. Ed.* **2014**, *53*, 10394.
[29] S. F. Plappert, J. M. Nedelec, H. Rennhofer, H. C. Lichtenegger, F. W. Liebner, *Chem. Mater.* **2017**, *29*, 6630.
[30] E. Abraham, V. Cherpak, B. Senyuk, J. Bart ten Hove, T. Lee, Q. Liu, I. I. Smalyukh, *Nat. Energy* **2023**, *8*, 381.
[31] M. S. Toivonen, A. Kaskela, O. J. Rojas, E. I. Kauppinen, O. Ikkala, *Adv. Funct. Mater.* **2015**, *25*, 6618.
[32] M. Lian, W. Ding, S. Liu, Y. Wang, T. Zhu, Y. E. Miao, C. Zhang, T. Liu, *Nano-Micro Lett.* **2024**, *16*, 131.
[33] S. Sen, J. D. Martin, D. S. Argyropoulos, *ACS Sustainable Chem. Eng.* **2013**, *1*, 858.
[34] M. Schestakow, I. Karadagli, L. Ratke, *Carbohydr. Polym.* **2016**, *137*, 642.
[35] A. Rege, M. Schestakow, I. Karadagli, L. Ratke, M. Itskov, *Soft Matter* **2016**, *12*, 7079.
[36] G. Nie, Y. Zang, W. Yue, M. Wang, A. Baride, A. Sigdel, S. Janaswamy, *Carbohydr. Polym. Technol. Appl.* **2021**, *2*, 100074.
[37] Q. Xu, C. Chen, K. Rosswurm, T. Yao, S. Janaswamy, *Carbohydr. Polym.* **2016**,*149*, 274.
[38] S. Zhou, K. Guo, D. Bukhvalov, X. Zhang, W. Zhu, J. Yao, M. He, *Adv. Mater. Technol.* **2020**, *5*, 2000358.
[39] R. Wang, C. Chen, Z. Pang, X. Wang, Y. Zhou, Q. Dong, M. Guo, J. U. Ray, Q. Xia, Z. Lin, S. He, B. Foster, T. Li, L. Hu, *Nano Lett.* **2022**, *22*, 3938.
[40] G. Horvat, M. Pantić, Ž. Knez, Z. Novak, *Gels* **2022**, *8*, 438.
[41] M. Thommes, K. Kaneko, A. Neimark, J. Olivier, F. Rodriguez-Reinoso, J. Rouquerol, K. Sing, *Pure Appl. Chem.* **2015**, *87*, 1051.
[42] A. Rege, I. Preibisch, M. Schestakow, K. Ganesan, P. Gurikov, B. Milow, I. Smirnova, M. Itskov, *Materials (Basel)* **2018**, *11*, 1670.
[43] K. Ganesan, L. Ratke, *Soft Matter* **2014**, *10*, 3218.
[44] S. Hoepfner, L. Ratke, B. Milow, *Cellulose* **2008**, *15*, 121.
[45] J. P. Llewellyn, F. Rouquerol in "*Characterization of Porous Solids VII", Studies in Surface Science and Catalysis*, (Eds: P. Llewellyn, F. Rodriguez-Reinoso, J. Rouquerol, N. Seaton), Elsevier, Amsterdam and Oxford, 49–56.
[46] A. Galarneau, F. Villemot, J. Rodriguez, F. Fajula, B. Coasne, *Langmuir* **2014**, *30*, 13266.
[47] C. Scherdel, G. Reichenauer, M. Wiener, *Microporous Mesoporous Mater.* **2010**, *132*, 572.
[48] L. Zhao, S. Yang, B. Bhatia, E. Strobach, E. N. Wang, *AIP Adv.* **2016**, *6*, 025123.
[49] B. Merillas, J. Mart, F. Villafañe, Á. Miguel, *Nanomaterials* **2022**, *12*, 1522.

[50] A. J. Hunt, *J. Non-Cryst. Solids* **1998**, *225*, 303.
[51] A. Wolf, B. Terheiden, R. Brendel, *J. Appl. Phys.* **2008**, *104*, 033106.
[52] H. Gratz, A. Penzkofer, P. Weidner, *J. Non. Cryst. Solids* **1995**, *189*, 50.
[53] J. Martín-de León, J. L. Pura, V. Bernardo, M. Á. Rodríguez-Pérez, *Polymer* **2019**, *170*, 16.
[54] W. J. Malfait, H. P Ebert, S. Brunner, J. Wernery, S. Galmarini, S. Zhao, G. Reichenauer, *J. Sol-Gel Sci. Technol.* **2024**, *109*, 569.
[55] I. Karadagli, B. Schulz, M. Schestakow, B. Milow, T. Gries, L. Ratke, *J. Supercritical Fluids* **2015**, *106*, 105.
[56] T. Woignier, J. Primera, A. Alaoui, F. Despetis, S. C. Etienne, A. Faivre, L. Duffours, C. Levelut, P. Etienne, *J. Sol-Gel Sci. Technol.* **2020**, *93*, 6.
[57] H. Xu, J. L. S. Salvador, A. Blanco, A. Balea, C. Negro, *Carbohydr. Polym.* **2023**, *319*, 121168.